Optical injection and control in germanium: Thirty-band k·p theory

J. Rioux and J. E. Sipe
Department of Physics and Institute for Optical Sciences, University of Toronto, 60 St. George Street, Toronto, Ontario, Canada M5S 1A7
(Received 11 September 2009; published 29 April 2010)

The optical injection of spin, current, and spin current in bulk Ge is investigated theoretically. Spin-polarized carriers can be photoexcited by monochromatic circularly polarized light through either one- or two-photon processes. With simultaneous ω and 2ω irradiation, currents can be injected and coherently controlled by interference of one- and two-photon transition amplitudes. We calculate the spectral dependence of these all-optical effects, including anisotropy and dichroism effects and a careful description of the hole spin injection. Injection at the E_1 resonance is studied thanks to an adaptive grid and a full-zone $\mathbf{k}\cdot\mathbf{p}$ band structure.

DOI: 10.1103/PhysRevB.81.155215 PACS number(s): 72.25.Fe, 72.40.+w, 42.65.−k, 78.20.−e

I. INTRODUCTION

Germanium is between gallium and arsenide in the periodic table, and so the properties of Ge and GaAs naturally exhibit many similarities. Indeed, in simple models of the band structure of GaAs near the center of the Brillouin zone the difference between the Ga and As atoms is neglected, in which case the lattice structure of GaAs (zinc blende) is identical to that of Ge (diamond), and there is no qualitative difference between the band structures of the two semiconductors. Of course, in more accurate models and calculations there are crucial differences. Since there is no center-of-inversion symmetry in GaAs the crystal can exhibit second-order nonlinear optical effects while Ge cannot: certain interband momentum matrix elements have different symmetry constraints in Ge than in GaAs; and GaAs is a direct band-gap semiconductor while in Ge the conduction-band minimum occurs at the L point rather than at the center of the Brillouin zone, and the gap is indirect.

This last effect leads to important differences in the behavior of optically injected carriers. In Ge the scattering to the side valleys at the L points is an effective relaxation process for electrons injected near the Γ point; this process does not exist in GaAs. While in GaAs the spin-relaxation times for holes are typically much shorter than those for electrons,[1,2] it is not clear how this scattering channel will affect the spin dynamics of injected electrons in Ge, and whether or not the injected hole spins might play a more dominant role in the spin dynamics of Ge than they do in GaAs. Current experimental work is underway to address this point.[3,4] In any case, the loss of injected electrons from the Γ region should make it easier to study the hole dynamics and the hole spin polarization in Ge, via pump-probe experiments, than it is to study them in GaAs; the direct-gap energy of Ge, which is only slightly higher than its indirect minimum gap, lies within the optical regime.

Thus the optical injection of carriers—both electrons and holes—is interesting from the point of view of fundamental physics, and with respect to possible applications in spintronics, where one seeks to use the spin degree of freedom of carriers to transport information.[5,6] Indeed, even if only its electrons were considered, Ge would be an interesting material to study. For its most abundant isotope has a spinless nucleus, reducing electron-spin decoherence, which is dominated by hyperfine interaction with nuclear spins.[5]

An important first step in any such program is the calculation of the injection of spin-polarized carriers, or "optical orientation," in Ge.[7] This can result from either one-photon absorption across the band gap or two-photon absorption with a sum photon energy greater than the band-gap energy. Contrary to the linear response, which is isotropic, two-photon absorption in diamond and zinc-blende materials exhibits anisotropy and dichroism.[8] Parameters of the two-photon absorption coefficient have been calculated for GaAs (Refs. 9–11) and Ge,[12,13] but there still seems to be disagreement in measured values for Ge,[14–16] as pointed out by Rauscher and Laenen.[16]

As well, the optical control of injected carriers is also of interest. It has been shown that carrier motion can be controlled in bulk semiconductors by irradiation with a "two-color field," containing a fundamental carrier frequency and its second harmonic; carriers are injected with a net average velocity from an interference of one- and two-photon transition amplitudes.[17] Such "1+2" effects have been experimentally observed in GaAs (Refs. 18–20) and Ge.[21] By taking advantage of spin-orbit splitting in the valence bands, spin-polarized and pure spin currents have been injected in GaAs.[22–25] While a recent experiment reports the detection of optically injected pure spin current in Ge,[3] that semiconductor has been the subject of many fewer studies than GaAs.

Motivated by the promise of interesting and novel electron and hole spin dynamics in Ge, in this paper we describe and calculate the spin, current, and spin-current injection in bulk Ge. We focus exclusively on direct absorption processes, neglecting the much weaker indirect, phonon-assisted processes that can occur at transition energies slightly less than the direct gap. Because of the $\Gamma \rightarrow L$ scattering present in Ge but absent in GaAs, it is likely that both electron and hole spin dynamics will be important; thus we pay equal attention to the contribution of both these carriers to spin injection. We also offer some comparisons with GaAs to address the issue of whether an effect is universal among cubic crystals or particular to a specific material. To compute optical properties, we use readily available 30-band $\mathbf{k}\cdot\mathbf{p}$ band structures.[26] Various $\mathbf{k}\cdot\mathbf{p}$ models with a 14-state basis have been successfully used in calculations of optical responses of semiconductors.[9,27–30] However, the accuracy of such band structures is limited to a range of roughly 0.5 eV above and below the semiconducting band gap, thus limiting their usefulness. A number of band structure features evidenced by

experimental data, such as the joint density of states responsible for the E_1 optical absorption edge, are simply missing in 14-band $\mathbf{k}\cdot\mathbf{p}$ models. Extending the basis to 30 states allows the correct description of the highest valence bands and lowest conduction bands in a range of over 10 eV.[26] This allows the prediction of optical responses at photon energies well above the 0.5 eV window.

In Sec. II of this paper, we describe the details of the 30-band $\mathbf{k}\cdot\mathbf{p}$ model. We use the $\mathbf{k}\cdot\mathbf{p}$ band structure as a basis for the calculations in the following sections. In Sec. III, we present carrier- and spin-injection calculations for both one- and two-photon absorption. We then study 1+2 interference currents and coherent control in Sec. IV. Our results are summarized in Sec. V.

II. MODEL

We consider the one-electron Schrödinger equation for an eigenstate ψ subject to the Hamiltonian $H=H_0+H_{S\text{-}O}$. The Hamiltonian H_0 includes a periodic potential $V(\mathbf{r})$ attributable to the crystalline structure, $H_0=p^2/2m+V(\mathbf{r})$, and $H_{S\text{-}O}$ is the spin-orbit interaction

$$H_{S\text{-}O}=\frac{1}{2m^2c^2}\mathbf{S}\cdot(\boldsymbol{\nabla}V\times\mathbf{p}), \tag{1}$$

where $\mathbf{S}$ and $\mathbf{p}$ are spin and momentum operators, m is the electron mass, and c is the speed of light in vacuum. In Eq. (1), we have neglected relativistic corrections proportional to $|\mathbf{S}\times\boldsymbol{\nabla}V|^2$.[29]

The coordinate representation of the eigenstates of H are Bloch functions, $\psi_{n\mathbf{k}}(\mathbf{r})=e^{i\mathbf{k}\cdot\mathbf{r}}u_{n\mathbf{k}}(\mathbf{r})$, products of plane waves and lattice periodic functions $u_{n\mathbf{k}}(\mathbf{r})$, with energy eigenvalue $\hbar\omega_n(\mathbf{k})$. The band index is denoted by n and $\mathbf{k}$ is the wave vector. The periodic u functions obey the $\mathbf{k}\cdot\mathbf{p}$ Hamiltonian

$$H_{\mathbf{k}}=H_0+H_{S\text{-}O}+\frac{\hbar^2k^2}{2m}+\frac{\hbar}{m}\mathbf{k}\cdot\mathbf{p}. \tag{2}$$

If known, the eigenstates at $\mathbf{k}=0$ serve as an infinite basis for expansion of the eigenstates of $H_{\mathbf{k}}$. However, in practice this expansion is limited to a manageable number of states. The basis states used are those closest in energy to the band gap at the Γ point. Their transformation properties can be determined by the symmetry of the lattice. Germanium belongs to the O_h symmetry group of cubic, centrosymmetric materials.

A. Thirty-band model

A set of 30 Γ-point states is used as a basis to expand eigenstates of the $\mathbf{k}\cdot\mathbf{p}$ Hamiltonian (2). The states are given by Richard *et al.*[26] and shown schematically in Fig. 1. The basis is an extension of the 15-band model of Cardona and Pollak[31] by direct product with the eigenstates of S^z. In this paper, we use the O_h double-group notation even for GaAs, unless it is otherwise noted. In addition to the states used in a 14-band model, the model used here introduces four upper conduction levels: two s-like states (Γ^+_{6u} and Γ^-_{7q}), a p-like multiplet ($\Gamma^+_{7d/8d}$), and Γ^-_{8d}, which is a doubly degenerate level (fourfold degenerate if counting spin) associated with d-like atomic functions that have the symmetry of $D_z=3z^2-r^2$ and $D_x=\sqrt{3}(x^2-y^2)$. Another s-like valence state (Γ^+_{6v}) is also added.

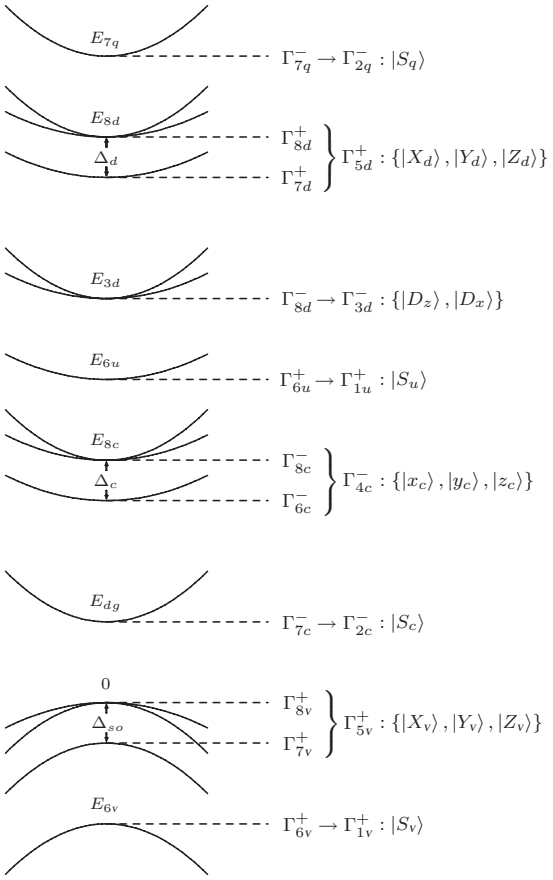

FIG. 1. Diagram of the states included in the 30-band model. Bands are labeled by zone-center energy and by Γ-point irreducible representations under the O_h double and simple group. To the right of the simple group notation are the basis states associated with that level.

B. Matrix elements

Under the symmetry operations of O_h, the momentum operator $\mathbf{p}$ transforms like Γ^-_4. Within the 30-state basis, independent momentum matrix elements are[32,33]

$$\langle S_c|p^x|X_v\rangle\equiv imP_0/\hbar, \tag{3a}$$

$$\langle S_c|p^x|X_d\rangle\equiv imP_d/\hbar, \tag{3b}$$

$$\langle S_q|p^x|X_v\rangle\equiv imP_2/\hbar, \tag{3c}$$

$$\langle S_q|p^x|X_d\rangle\equiv imP_{2d}/\hbar, \tag{3d}$$

$$\langle D_z|p^x|X_v\rangle\equiv imP_3/\hbar, \tag{3e}$$

$$\langle D_z|p^x|X_d\rangle\equiv imP_{3d}/\hbar, \tag{3f}$$

$$\langle S_v|p^x|x_c\rangle\equiv imP_s/\hbar, \tag{3g}$$

$$\langle X_v|p^y|z_c\rangle\equiv imQ_{vc}/\hbar, \tag{3h}$$

TABLE I. Material parameters.

(eV)	Ge	GaAs	(eV)	Ge	GaAs	(eV Å)	Ge	GaAs	(eV Å)	Ge	GaAs
E_{7q}	18.36	13.64	E_{6v}	−13.14	−12.55	P_0	9.681	9.232	P_d	−0.139	0.195
E_{8d}	17.0	11.89	Δ_{so}	0.290	0.341	P_2	3.092	4.891	P_{2d}	10.253	9.392
E_{3d}	10.47	10.17	Δ_{vd}	0.250	0.211	P_3	4.456	4.328	P_{3d}	7.749	5.819
E_{6u}	7.77	8.56	Δ_c	0.210	0.081	P_s	2.020	3.045	Q_{vc}	8.200	7.998
E_{8c}	3.22	4.569	Δ_d, Δ_{3c}	0	0	P_u	8.244	8.648	Q_{cd}	6.826	4.068
E_{dg}	0.90	1.519				P'		0.500			

$$\langle S_u|p^x|x_c\rangle \equiv imP_u/\hbar, \tag{3i}$$

$$\langle x_c|p^y|Z_d\rangle \equiv imQ_{cd}/\hbar. \tag{3j}$$

The spin-orbit coupling instead has the symmetry Γ_4^+ with independent terms

$$\langle X_v|(\nabla V\times \mathbf{p})^y|Z_v\rangle \equiv i\frac{4m^2c^2}{3\hbar}\Delta_{so}, \tag{4a}$$

$$\langle x_c|(\nabla V\times \mathbf{p})^y|z_c\rangle \equiv i\frac{4m^2c^2}{3\hbar}\Delta_{c}, \tag{4b}$$

$$\langle X_d|(\nabla V\times \mathbf{p})^y|Z_d\rangle \equiv i\frac{4m^2c^2}{3\hbar}\Delta_{d}, \tag{4c}$$

$$\langle X_v|(\nabla V\times \mathbf{p})^y|Z_d\rangle \equiv i\frac{4m^2c^2}{3\hbar}\Delta_{vd}. \tag{4d}$$

The states D_z and D_x also couple with the $\Gamma^-_{6c/8c}$ multiplet through the spin-orbit term[34]

$$\langle D_z|(\nabla V\times \mathbf{p})^x|x_c\rangle \equiv i\frac{4m^2c^2}{3\hbar}\Delta_{3c}. \tag{4e}$$

The P's, Q's, and Δ's are real parameters defined by these equations. The values that we use in this paper are those of Richard *et al.*,[26] reproduced for Ge and GaAs in Table I. For noncentrosymmetric materials, there exist, in principle, a number of additional nonzero matrix elements due to the lower symmetry. However, in order to describe GaAs, Richard *et al.* found it sufficient to introduce only one additional momentum parameter: $P'\equiv(-i\hbar/m)\langle S_c|p^x|x_c\rangle$. Other terms are left null, including the spin-orbit coupling Δ' (some authors denote this by $\bar{\Delta}$ or Δ^-) connecting $\{|x_c\rangle,|y_c\rangle,|z_c\rangle\}$ with $\{|X_v\rangle,|Y_v\rangle,|Z_v\rangle\}$.[35]

C. Computational details

The validity of calculations using the 30-band model has been addressed in a recent comparison with density-functional theory.[39] We prefer the present $\mathbf{k}\cdot\mathbf{p}$ approach over an *ab initio* treatment for two main reasons. First, computational times, both overhead and per $\mathbf{k}$ point, are significantly less in a $\mathbf{k}\cdot\mathbf{p}$ calculation than in even a local-density-approximation calculation. Second, the underestimation of the band-gap characteristic of density-functional-theory calculations is particularly significant in Ge; "scissors" corrected band structures give poor fits to the actual band features close to the Γ point, and more sophisticated many-body extensions to this simple strategy require much more computation.[40,41]

All calculations employ the independent particle approximation, associating the perturbing electric field used in the response calculations with the Maxwell field in the medium. Many-body effects and the consequences of phonon scattering are neglected throughout. In particular, optical absorption across the indirect gap of germanium—possible with the contribution of crystal momentum from phonon scattering—is neglected. This effect is much weaker than direct absorption, although it dominates the linear optical response for photon energy in the range $E_{ig}<\hbar\omega<E_{dg}$, where, at zero temperature, the indirect and direct energy gaps are $E_{ig}=0.744$ eV and $E_{dg}=0.898$ eV.[42]

A difficulty that arises in any band-structure calculation is the problem of efficient $\mathbf{k}$-point sampling when performing numerical integration. We find that a few spectral features of the injection tensors require a significant number of $\mathbf{k}$ points in order to resolve them numerically. We use the reduction method of Blöchl *et al.*[43] and an adaptive refinement technique to produce an irreducible wedge covering the equivalent of the full Brillouin zone at various degrees of coarseness. The resulting grid uses 90 124 $\mathbf{k}$ points; the finest region, at the zone center, is covered by an effective $1280\times1280\times1280$ grid. We perform integration by linearly interpolating integrands and energies over tetrahedral volume elements. The details of the refinement and integration steps are described elsewhere.[39]

III. CARRIER AND SPIN INJECTION

A. One-photon process

In this section, we present microscopic calculations of spin injection. We initially consider the linear response of the semiconductor to a monochromatic field of frequency ω

$$\mathbf{E}(t)=\mathbf{E}(\omega)e^{-i\omega t}+\text{c.c.} \tag{5}$$

with $\hbar\omega$ greater than the direct band-gap energy E_{dg}. The rate of one-photon spin injection $\dot{\mathbf{S}}_1$ is

$$\dot{S}_1^a(\omega)=\zeta_1^{abc}(\omega)E^b(-\omega)E^c(\omega). \tag{6}$$

In this paper, Roman superscripts indicate Cartesian components along the cubic axes; summation over repeated indices

is implied. A standard Fermi's golden-rule (FGR) derivation of $\zeta_1^{abc}(\omega)$ neglects coherences between nearly degenerate excited states. Because the bandwidth of a typical laser can excite superpositions of states, such coherences must be included to capture the physics. We follow a multiple-scale approach, in the manner of Nastos *et al.*,[39] to obtain an expression for $\zeta_1^{abc}(\omega)=\zeta_{1;e}^{abc}(\omega)+\zeta_{1;h}^{abc}(\omega)$ including coherences. The electron contribution $\zeta_{1;e}^{abc}(\omega)$ and the hole contribution $\zeta_{1;h}^{abc}(\omega)$ are given by

$$\underset{(h)}{\zeta_{1;e}^{abc}}(\omega)=(-)\frac{\pi e^2}{\hbar^2\omega^2}\sum_{(c,v,v')}^{c,c',v}{}'\int\frac{d^3k}{8\pi^3}\underset{(v'v)}{S^{a}_{cc'}}(\mathbf{k})v_{cv}^{b*}(\mathbf{k})\underset{(cv')}{v^{c}_{c'v}}(\mathbf{k})$$
$$\times(\delta[\omega_{cv}(\mathbf{k})-\omega]+\delta[\underset{(cv')}{\omega_{c'v}}(\mathbf{k})-\omega]),\tag{7}$$

where throughout this paper we take $e=-|e|$ to be the charge of the electron. For a given band m, the Bloch state $|m\mathbf{k}\rangle$ has energy eigenvalue $\hbar\omega_m(\mathbf{k})$. The quantities $\mathbf{v}_{mn}(\mathbf{k})$ and $\mathbf{S}_{mn}(\mathbf{k})$ denote the matrix elements of the velocity and spin operators between bands m and n at wave vector $\mathbf{k}$

$$\langle m\mathbf{k}|\mathbf{v}|n\mathbf{k}'\rangle=\mathbf{v}_{mn}(\mathbf{k})\delta(\mathbf{k}-\mathbf{k}'),\tag{8}$$

$$\langle m\mathbf{k}|\mathbf{S}|n\mathbf{k}'\rangle=\mathbf{S}_{mn}(\mathbf{k})\delta(\mathbf{k}-\mathbf{k}').\tag{9}$$

When evaluating the velocity operator, we neglect the anomalous part arising from spin-orbit coupling.[29] We use the definitions $\omega_{mn}(\mathbf{k})\equiv\omega_m(\mathbf{k})-\omega_n(\mathbf{k})$ and, later in this paper, $\bar{\omega}_{mn}(\mathbf{k})\equiv[\omega_m(\mathbf{k})+\omega_n(\mathbf{k})]/2$. When a band index c or v is used, it is understood that the corresponding summation is restricted only to conduction or valence bands, respectively. The prime on the summation in Eq. (7) indicates an additional restriction to degenerate or quasidegenerate pairs of states for which $|\omega_{cc'}|$ (or $|\omega_{vv'}|$) $<\epsilon_{\text{cut}}/\hbar$. The cutoff value of $\epsilon_{\text{cut}}=30$ meV is chosen because it matches both k_BT at room temperature and a typical laser linewidth.[39] Its repercussions on the results are discussed below.

The macroscopic spin injection $\dot{\mathbf{S}}$ could be due to a large number of weakly polarized carriers or a few highly polarized ones. To distinguish between these two cases, we use a measure of the average spin per carrier, or the degree of spin polarization (DSP), defined by

$$\text{DSP}^a=\frac{\dot{S}^a}{\frac{\hbar}{2}\dot{n}},\tag{10}$$

where $\dot{n}$ is the carrier injection rate. From FGR or from a multiple-scale derivation, the one-photon absorption rate is given by

$$\dot{n}_1(\omega)=\xi_1^{ab}(\omega)E^a(-\omega)E^b(\omega)\tag{11}$$

with

$$\xi_1^{ab}(\omega)=\frac{2\pi e^2}{\hbar^2\omega^2}\sum_{c,v}\int\frac{d^3k}{8\pi^3}v_{cv}^{a*}(\mathbf{k})v_{cv}^{b}(\mathbf{k})\delta[\omega_{cv}(\mathbf{k})-\omega].\tag{12}$$

For diamond and zinc-blende crystal structures, a single independent component of the carrier-injection tensor exists:

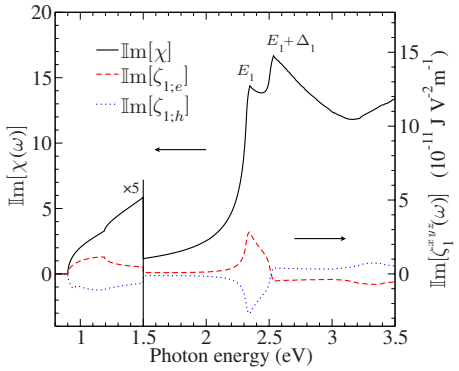

FIG. 2. (Color online) The linear response of Ge as a function of photon energy $\hbar\omega$, computed from the 30-band $\mathbf{k}\cdot\mathbf{p}$ model. The imaginary part of the susceptibility $\chi(\omega)$ is shown in black with the E_1 and $E_1+\Delta_1$ absorption features identified. The dashed red (dotted blue) curve shows the electron (hole) spin-injection component $\zeta_1^{xyz}(\omega)$. The scale is such that the DSP can be read off by taking the ratio of both quantities. Although expressions in the text are given in the Gaussian system, all plots use SI units.

$\xi_1^{xx}=\xi_1^{yy}=\xi_1^{zz}$. It is related to the susceptibility of the material by $\mathbb{I}\mathrm{m}[\chi(\omega)]=\frac{\hbar}{2}\xi_1(\omega)$. The spin-injection pseudotensor also has an unique independent component: $\zeta_1^{xyz}=\zeta_1^{yzx}=\zeta_1^{zxy}=-\zeta_1^{xzy}=-\zeta_1^{yxz}=-\zeta_1^{zyx}$. Within the independent particle approximation, the quantities ξ_1^{xx} and ζ_1^{xyz} are, respectively, purely real and purely imaginary; $\chi(\omega)$ and $\zeta_1(\omega)$ are plotted for Ge in Fig. 2.

As a sample calculation, we consider an optical field which is left-circularly polarized and propagating along the $-\hat{\mathbf{z}}$ direction, where x, y, and z describe three general mutually orthogonal right-handed axes, so that $\mathbf{E}(\omega)=E_0\hat{\boldsymbol{\sigma}}^-$, where E_0 is the field amplitude and $\hat{\boldsymbol{\sigma}}^{\pm}=(\hat{\mathbf{x}}\pm i\hat{\mathbf{y}})/\sqrt{2}$. We find that injected spins are parallel to the z axis, independent of how the laboratory coordinate system is oriented with respect to crystallographic axes. The degree of spin polarization is given by $\text{DSP}^z(\omega)=(\hbar/2)^{-1}\mathbb{I}\mathrm{m}[\zeta_1^{xyz}(\omega)]/\xi_1^{xx}(\omega)$ and is shown in Fig. 3.

At the onset of absorption, injected electrons are 50% spin polarized. Such a value as been calculated for GaAs and can be understood from the atomiclike states involved in the Γ-point transitions.[39] The top-valence and bottom-conduction bands of Ge share the same character as those of GaAs (Fig. 4). The smaller band gap explains a shift of the spectrum toward lower photon energies. The states involved and the transition amplitudes are presented in Fig. 4(a).

As the photon energy is increased, the DSP of electrons drops but remains above 40% over a range of energy corresponding to the spin-orbit splitting in the valence bands (290 meV in Ge). At photon energy greater than 1.2 eV, the spin polarization is reduced to as low as 10%. This results from a combination of the onset of absorption from the split-off band and a drop in the polarization from the light-hole-mediated transition. A similar behavior has been seen in spin-injection calculations in GaAs.[39] Spin injection is enhanced again near 2.3 eV, which corresponds to the E_1 absorption edge (*cf.* Fig. 2). This stems from a high joint density of states between conduction and heavy-hole bands in the Γ-L valley of the Brillouin zone.[44]

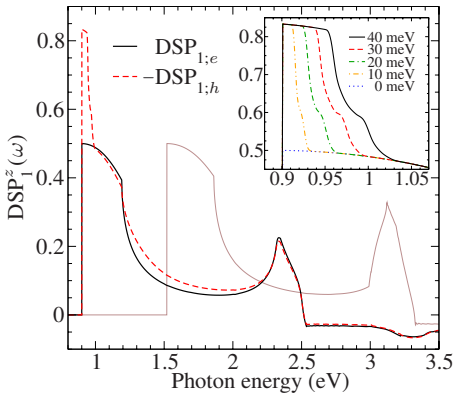

FIG. 3. (Color online) The degree of spin polarization of carriers optically injected in Ge by left-circularly polarized light. The plain black (dashed red) curve shows the electron (hole) spin. Electron spin polarization in GaAs is shown in a thin brown line for reference. Inset: DSP of the holes for different values of the cut-off energy ϵ_{cut}.

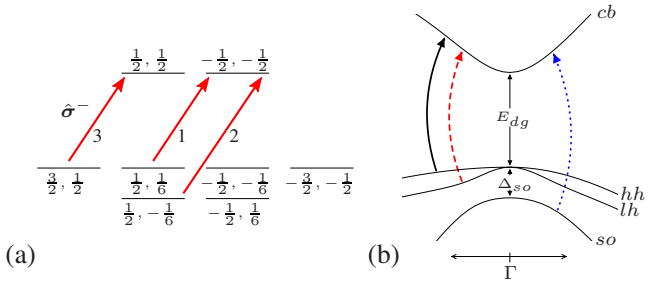

FIG. 4. (Color online) (a) Γ-point states contributing to spin injection. The electron energy levels are labeled by the expectation values $\langle J^z\rangle$ and $\langle S^z\rangle$, in units of $\hbar$, within those states. The solid red arrows show the transitions induced by left-circularly polarized light. Each adjacent number is the relative strength of that transition at the onset of absorption. (b) Band structure near the zone center. Optical transitions are identified by arrows as follow: plain black, dashed red, and dotted blue curves correspond to the excitation of electrons from the heavy, light, and split-off valence bands, respectively.

Optically injected holes have a spin polarization which is mostly opposite that of the electrons. At the band edge, however, the degree of hole spin polarization is −83.3%. This value can be understood from the Γ-point states alone. As shown in the diagram of Fig. 4(a), circularly polarized light excites electrons from the $\langle J^z\rangle=3\hbar/2$ and $\langle J^z\rangle=\hbar/2$ valence states in a ratio of 3:1. The expectation value of S^z within those electronic states is respectively $\hbar/2$ and $\hbar/6$, leaving holes which are spin polarized by

$$\frac{3\left(-\frac{\hbar}{2}\right)+1\left(-\frac{\hbar}{6}\right)}{(\hbar/2)(3+1)}=-\frac{5}{6}$$

or −83.3%. Thus at the onset of absorption, where coherences between heavy- and light-hole bands are excited, the injected holes are significantly more spin polarized than the electrons.

The DSP of the holes is decomposed into contributions from different transitions in Fig. 5. Holes injected in the heavy- and light-hole bands are both −83.3% spin polarized at the band-gap energy. The strong polarization survives increasing photon energy until the heavy- and light-hole band splitting reaches the cutoff energy $\epsilon_{\text{cut}}=30$ meV, at which point we are no longer keeping the coherences between states. This corresponds to excitations into the heavy- and light-hole bands that are roughly 50 and 80 meV, respectively, above the absorption edge. Two significant drops in polarization occur at those energies. Note that the value of 30 meV is a nominal number; what is observed close to the fundamental absorption edge ultimately depends on the bandwidth and other properties of the laser, as well as relaxation processes (*cf*. the inset of Fig. 3). At the onset of injection into the split-off band, −33.3% spin-polarized holes are excited, whereas the light-hole contribution drops and even changes sign. A similar decomposition of the electron spin by transition gives an almost identical result as GaAs (with corresponding shifts in the band-gap and split-off energies) and its presentation is omitted here (*cf*. Fig. 6 of Nastos *et al.*[39]).

B. Two-photon process

Two-photon carrier- and spin-injection processes occur at rates proportional to the square of the intensity of the incident field rather than at rates linearly proportional to the intensity characteristic of one-photon injection processes. The second-order responses are

$$\dot{n}_2(\omega)=\xi_2^{abcd}(\omega)E^a(-\omega)E^b(-\omega)E^c(\omega)E^d(\omega), \quad (13)$$

$$\dot{S}_2^a(\omega)=\zeta_2^{abcde}(\omega)E^b(-\omega)E^c(-\omega)E^d(\omega)E^e(\omega). \quad (14)$$

The fifth-rank pseudotensor $\zeta_2^{abcde}(\omega)$ and fourth-rank tensor $\xi_2^{abcd}(\omega)$ describe two-photon spin and carrier injection, respectively. The latter is related to the degenerate part of $\chi^{(3)}$, the third-order nonlinear susceptibility, by $\mathbb{I}\text{m}[\chi^{(3)}(\omega;-\omega,\omega,\omega)]=\frac{\hbar}{3}\xi_2(\omega)$. From a microscopic derivation, either using FGR (as in van Driel and Sipe[45]) or the more general multiple-scale approach, it is given by

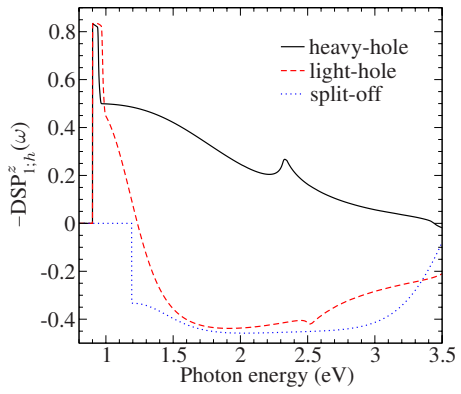

FIG. 5. (Color online) Decomposition of the degree of hole spin polarization by transitions involving different states. The transitions are identified in Fig. 4(b).

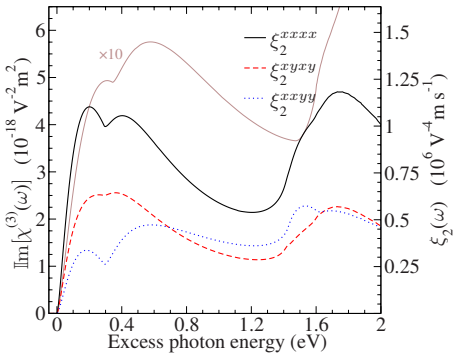

FIG. 6. (Color online) Imaginary part of the degenerate third-order nonlinear susceptibility $\chi^{(3)}(\omega;-\omega,\omega,\omega)$, in relation to the two-photon injection tensor $\xi_2(\omega)$. Black, dashed red, and dotted blue curves: independent components of ξ_2^{abcd} in Ge; thin brown curve: ξ_2^{xxxx} in GaAs. The horizontal axis uses excess photon energy, defined as $2\hbar\omega - E_{dg}$; the direct-gap energy is 0.9 eV for Ge and 1.519 eV for GaAs.

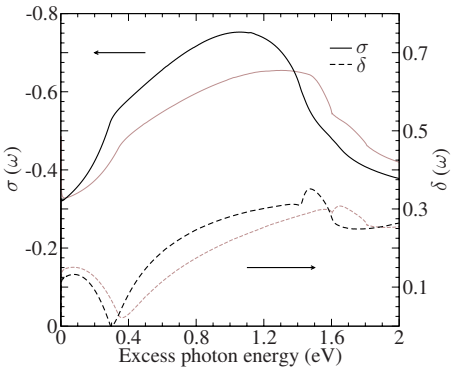

FIG. 7. (Color online) Anisotropy $\sigma(\omega)$ and linear-circular dichroism $\delta(\omega)$ of the two-photon absorption in Ge (thick black curves) and GaAs (thin brown curves).

$$\xi_2^{abcd}(\omega) = \frac{2\pi e^4}{\hbar^4\omega^4}\sum_{c,v}\int \frac{d^3k}{8\pi^3} w_{cv}^{ab*}(\mathbf{k}) w_{cv}^{cd}(\mathbf{k}) \times \delta[\omega_{cv}(\mathbf{k}) - 2\omega], \tag{15}$$

where we define

$$w_{cv}^{ab}(\mathbf{k}) \equiv \frac{1}{2}\sum_m \frac{v_{cm}^a(\mathbf{k}) v_{mv}^b(\mathbf{k}) + v_{cm}^b(\mathbf{k}) v_{mv}^a(\mathbf{k})}{\omega_m(\mathbf{k}) - \bar{\omega}_{cv}(\mathbf{k})}. \tag{16}$$

The quantity $w_{vc}^{ab}(\mathbf{k})$ is essentially the degenerate two-photon transition amplitude. Without loss of generality, Eq. (16) has been explicitly symmetrized with respect to the interchange of Cartesian superscripts; they refer to the same electric field component.

The two-photon injection tensor $\xi_2^{abcd}(\omega)$ is purely real within the independent particle approximation and has three independent components: ξ_2^{xxxx}, ξ_2^{xxyy}, and ξ_2^{xyxy}. In total, 21 nonzero components are formed by cyclic permutations of Cartesian directions, or by exchanging $a \leftrightarrow b$, $c \leftrightarrow d$, or $ab \leftrightarrow cd$. In an isotropic model, only two of these components are independent; we have $\xi_2^{xxxx} = 2\xi_2^{xyxy} + \xi_2^{xxyy}$.[10] The 30-band model gives access to additional bands whose warping effects on the valence bands of Ge creates anisotropy in the two-photon absorption. Hutchings and Wherrett[9] presented two parameters, the anisotropy σ and the linear-circular dichroism δ, to characterize those effects

$$\sigma = \frac{\xi_2^{xxxx} - 2\xi_2^{xyxy} - \xi_2^{xxyy}}{\xi_2^{xxxx}}, \tag{17}$$

$$\delta = \frac{\xi_2^{xxxx} - 2\xi_2^{xyxy} + \xi_2^{xxyy}}{2\xi_2^{xxxx}}. \tag{18}$$

In the isotropic limit, $\sigma = 0$ and $\delta = \xi_2^{xxyy}/\xi_2^{xxxx}$.[10] We plot the independent components of the two-photon absorption tensor in Fig. 6, and the anisotropy and linear-circular dichroism parameters in Fig. 7.

The onset of direct two-photon absorption occurs when $2\hbar\omega$ matches the direct energy gap. The edge at 0.29 eV marks the onset of absorption from the split-off band, a transition that is most sensitive to the field polarization; its effect on the $xyxy$ component is particularly small. These low-energy contributions are transitions taking place at the zone center that are dominated by allowed-forbidden processes. That is, one of the matrix elements appearing in Eq. (16) is nonvanishing at the Γ point (allowed) while the other vanishes there (forbidden) and only becomes nonzero as we move away from zone center. Within a parabolic-band approximation, the spectral dependence of these transitions is of the form $(2\hbar\omega - E_{dg})^{3/2}/(2\hbar\omega)^5$.[46] Although we go beyond this approximation with the 30-band model, these contributions retain this broad qualitative feature. The strong low-energy absorption in Ge relative to GaAs can be explained by the much smaller effective mass of conduction electrons in the former. At excess photon energies of 1.5 and 1.7 eV, two additional absorption edges are visible. These stem from high joint density of states for absorption from the heavy- and light-hole bands in the Γ-L valley. The same states are also responsible for the E_1 and $E_1 + \Delta_1$ peaks in the linear response (*cf.* Fig. 2).

For reasons described in Sec. III A, we use again a multiple-scale approach to derive the two-photon spin-injection pseudotensor. We obtain

$$\underset{(h)}{\zeta_{2;e}^{abcde}}(\omega) = (-)\frac{\pi e^4}{\hbar^4\omega^4}\sum_{\substack{c,c',v \\ (c,v,v')}}\int \frac{d^3k}{8\pi^3} \underset{(v'v)}{S_{cc'}^{a}}(\mathbf{k}) w_{cv}^{ab*}(\mathbf{k}) \underset{(cv')}{w_{c'v}^{cd}}(\mathbf{k}) \times (\delta[\omega_{cv}(\mathbf{k}) - 2\omega] + \delta[\underset{(cv')}{\omega_{c'v}}(\mathbf{k}) - 2\omega]), \tag{19}$$

reproducing the result that Bhat *et al.*[27] obtained from heuristic arguments. Within the independent particle approximation, $\zeta_2^{abcde}(\omega)$ is purely imaginary and has two independent components: $\zeta_2^{xxyxz} = -\zeta_2^{xxzxy}$ and $\zeta_2^{xyzzz} = \zeta_2^{xyyyz} = -\zeta_2^{xzzyz} = -\zeta_2^{xyzyy}$. All 48 nonzero elements can be related to ζ_2^{xyzzz} and ζ_2^{xxyxz} by cyclic permutations of the Cartesian directions, exchanging $b \leftrightarrow c$, exchanging $d \leftrightarrow e$, or any combination of these. We show electron and hole contributions to both components in Fig. 8.

Note that Eqs. (15) and (19) are derived under the assumption that there is no intermediate energy level exactly

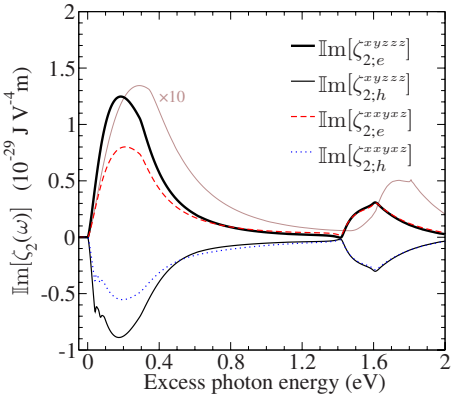

FIG. 8. (Color online) Components of the two-photon spin-injection pseudotensor $\zeta_2^{abcde}(\omega)$ in Ge. The thick black and dashed red curves are electronic contributions; plain black and dotted blue curves show the hole spin components. The fine structure seen near the onset of absorption in the lower two curves is due to the heavy- and light-hole band splitting. The thin brown curve shows $\mathbb{I}\mathrm{m}[\zeta_{2;e}^{xyzzz}]$ for the electrons of GaAs.

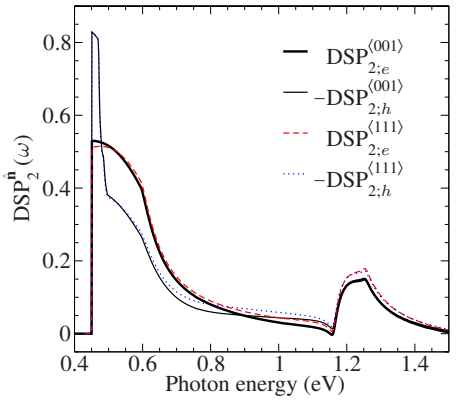

FIG. 9. (Color online) The degree of spin polarization of carriers optically injected by two-photon absorption in Ge. The thick (thin) black curve shows the electron (hole) spin for left-circularly polarized light at ⟨001⟩ incidence. Spin polarization at ⟨111⟩ incidence is shown in a dashed red line for electrons and a dotted blue line for holes.

midway between initial and final states of the absorption process. Therefore, in applying these formulas one has to be particularly careful at energies where $2\hbar\omega$ is sufficiently high above the gap that an intermediate state exists at an energy $\hbar\omega$ above the initial state. An investigation of the 30-band $\mathbf{k}\cdot\mathbf{p}$ band structure shows that the lowest photon energy at which this occurs is $\hbar\omega \approx 1.57$ eV, corresponding to an excess photon energy of 2.24 eV, and results from a small region of $\mathbf{k}$ space where the lowest conduction band of germanium is resonant with excitations from the heavy hole into the second conduction band. We have verified that no resonance occurs within the energy range we consider. In a more general theory, resonances could be included with a dressed-band approach, where the finite lifetime of the intermediate state would also have to be taken into account.[47]

For left-circularly polarized light incident on either a ⟨001⟩ or ⟨111⟩ direction, the injected spin polarization is antiparallel with the propagation axis, with degrees of spin polarization given by

$$\mathrm{DSP}_2^{\langle 001\rangle} = \frac{(\hbar/2)^{-1} 2\ \mathbb{I}\mathrm{m}[\zeta_2^{xyzzz}(\omega)]}{\xi_2^{xyxy}(\omega) - \frac{1}{2}\xi_2^{xyyy}(\omega) + \frac{1}{2}\xi_2^{xxxx}(\omega)},$$

$$\mathrm{DSP}_2^{\langle 111\rangle} = \frac{(\hbar/2)^{-1}\frac{4}{3}\mathbb{I}\mathrm{m}[\zeta_2^{xxyxz}(\omega) + \zeta_2^{xyzzz}(\omega)]}{\frac{4}{3}\left[\xi_2^{xyxy}(\omega) - \frac{1}{4}\xi_2^{xyyy}(\omega) + \frac{1}{4}\xi_2^{xxxx}(\omega)\right]}.$$

In terms of the anisotropy σ and dichroism δ, the denominators of these expressions are $\xi_2^{xxxx}(1-\delta)$ and $\xi_2^{xxxx}(1-\delta-\frac{1}{6}\sigma)$, respectively. The two-photon DSP is shown for both orientations in Fig. 9, as a function of the photon energy $\hbar\omega$. The electron spin polarization near the onset of absorption is enhanced by a few percent compared to the value of 50% obtained from linear absorption (*cf.* Fig. 3). Cubic anisotropy leads to only a small difference between the two orientations in the average spin per injected carrier.

For the holes, the DSP is again roughly $-5/6$ at the band edge. The drop due to heavy- and light-hole band splitting is more significant than in the linear process; once the two hole bands have an energy separation of 30 meV or more, the polarization falls sharply below −40%. On the other hand, the onset of absorption for transitions from the split-off band is not as pronounced. Although it does contribute to a decreasing DSP, this effect only reinforces a larger drop in polarization from the light-hole transitions. This is analogous to optical orientation under linear absorption (*cf.* Fig. 5). At larger photon energy, electron and hole polarizations are almost exactly opposite.

The DSP can be broken down into contributions arising from different intermediate states or levels by restricting the sum over m in Eq. (16). This is shown for both electron and hole spin polarization in Fig. 10. We distinguish between two-photon processes mediated by either the highest valence bands ($\Gamma_{7v/8v}^{+}$) or the lowest conduction band (Γ_{7c}^{-}). For the range of photon energy considered, these are two-band tran-

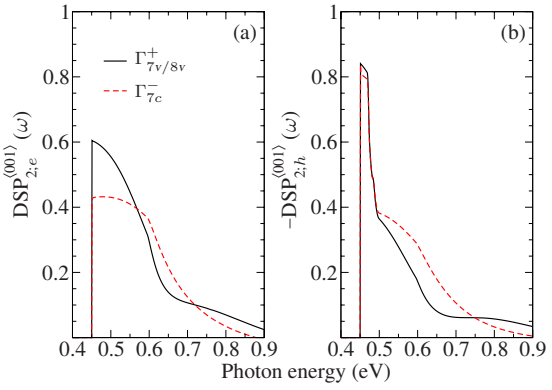

FIG. 10. (Color online) Decomposition by intermediate states for left-circularly polarized light incident on ⟨001⟩: two-photon DSP of (a) electrons and (b) holes.

sitions; the intermediate state belongs to the same subset as either the initial or final state. Two-band transitions are so-called allowed-forbidden (*a-f*) processes. One should not be misled by the name; the transition probability is truly zero only at the Γ point and, in fact, an energy-denominator argument favors such transitions. Consider, for example, the next-to-lowest conduction level ($\Gamma^-_{6c/8c}$) as intermediates. For noncentrosymmetric materials, this level ($\Gamma_{7c/8c}$ in T_d double-group notation) mediates the most energetically favorable allowed-allowed (*a-a*) transition. In GaAs, it lies 4.488 eV above the top of the valence band, or roughly three times the band-gap energy (1.519 eV). For $\hbar\omega$ on the order of the band gap, this means that the denominator of Eq. (16) is two to three times larger for this process than for a two-band process. Thus, even the most favorable *a-a* process dominates only very close to the band edge. Contributions from *a-f* processes mediated through either the initial or final state are otherwise more important.[48] For germanium, the aforementioned *a-a* process is in fact allowed forbidden since the momentum parameter P' vanishes identically under inversion symmetry. For this reason, Ge does not exhibit the type of variation in the two-photon DSP seen near the band-edge of inversion asymmetric crystals, typically over a range of 10 meV, reported by Bhat *et al.*[27] for GaAs and other III-V semiconductors.

Electrons injected with a transition mediated through the conduction band (dashed red curve in Fig. 10) have a DSP of roughly 40% at the band edge, compared to 60% for valence-band-mediated transitions (black curve). Complex transition rules within the valence level, which consists of split $J=3\hbar/2$- and $J=\hbar/2$-like sublevels, can explain the stronger spin polarization for the latter type of transitions. This supports the argument that the valence-band structure is crucial to the spin injection process. Above the onset of absorption, the DSP of carriers excited through valence-band mediation decreases with increasing photon energy due to band mixing among heavy- and light-hole bands. The DSP of conduction-band-mediated electrons, on the contrary, is not very sensitive to the substructure of these bands; it goes down by only a few percents over the same energy range. Both types of transitions suffer a significant drop in polarization at energies where the split-off band starts contributing.

IV. COHERENT CONTROL

In this section, we concern ourselves with the motion of optically injected carriers. Consider a semiconductor subjected to a two-color optical field

$$\mathbf{E}(t) = \mathbf{E}(\omega)e^{-i\omega t} + \mathbf{E}(2\omega)e^{-2i\omega t} + \text{c.c.} \tag{20}$$

consisting of monochromatic beams of frequency ω and 2ω. With such harmonically related components, one-photon absorption at 2ω matches two-photon absorption at ω. It has been shown that the interference of the probability amplitudes for the two processes leads to injected charge[17] and spin[22] currents, examples of so-called 1+2 interference. The total injection rate for carrier density is given by

$$\dot{n} = \dot{n}_1(2\omega) + \dot{n}_2(\omega), \tag{21}$$

where $\dot{n}_1$ is from one-photon absorption of the 2ω beam and $\dot{n}_2$ is from two-photon absorption of the ω beam with their respective expressions given in Eqs. (11) and (13). The carrier injection due to the interference of one- and two-photon absorption, often called population control, is zero for Ge due to center-of-inversion symmetry.[49]

Inversion symmetry also prohibits current injection in centrosymmetric materials from one-color processes alone. Rather, the source of current injection in those materials comes from the crossterm of one- and two-photon amplitudes. So, although 1+2 interference does not lead to population control, it is essential to coherently controlled current and spin-current injection in Ge.

A. Current injection

The charge current due to the crossterm of transition amplitudes from ω and 2ω beams has an injection rate given by

$$\dot{J}^a_I = \eta^{abcd}_I(\omega)E^b(-\omega)E^c(-\omega)E^d(2\omega) + \text{c.c.} \tag{22}$$

The fourth-rank tensor $\eta^{abcd}_I(\omega)$ includes contributions from both electrons and holes. An FGR derivation gives the microscopic expression[17]

$$\underset{(h)}{\eta^{abcd}_{I;e}}(\omega) = (-)\frac{i\pi e^4}{\hbar^3\omega^3}\sum_{c,v}\int \frac{d^3k}{8\pi^3} \underset{(vv)}{v^{\ a}_{cc}}(\mathbf{k}) w^{bc*}_{cv}(\mathbf{k}) v^d_{cv}(\mathbf{k}) \times \delta[\omega_{cv}(\mathbf{k}) - 2\omega]. \tag{23}$$

This expression sums the contributions to the current from each injected carrier. The first velocity matrix element above is from the expectation value of the current operator; its superscript corresponds to the direction of the current. The product of $w^{bc}_{vc}(\mathbf{k})$ and $v^d_{cv}(\mathbf{k})$ is directly related to the crossterm of two- and one-photon transition amplitudes, respectively. For zinc-blende and diamond structure crystals there are 21 nonzero components to $\eta^{abcd}_I(\omega)$, related—by the exchange $b\leftrightarrow c$, $ab\leftrightarrow cd$, and cyclic permutations of the indices—to only three independent components: η^{xxxx}_I, η^{xxyy}_I, and η^{xyyx}_I. They are plotted in Fig. 11 as a function of the energy $2\hbar\omega$ in excess of the direct energy gap.

B. Spin-current injection

Bhat and Sipe[22] have shown that upon excitation with the harmonically related two-color field of Eq. (20) a carrier population can be injected with a nonzero expectation value of the spin-current operator $K^{ab}=\langle v^a S^b\rangle$. Spin-current injection results from the interference of two-photon absorption at ω and one-photon absorption at 2ω. Explicitly

$$\dot{K}^{ab}_I = \mu^{abcde}_I(\omega)E^c(-\omega)E^d(-\omega)E^e(2\omega) + \text{c.c.} \tag{24}$$

The fifth-rank pseudotensor $\mu^{abcde}_I(\omega)$ includes electron and hole contributions. In order to properly treat coherences between excited states, we employ the multiple-scale approach, as in the spin-injection calculations of Sec. III. This yields

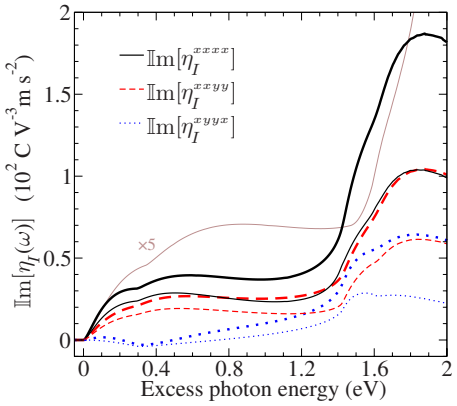

FIG. 11. (Color online) Components of $\eta_I^{abcd}(\omega)$, the 1+2 current-injection tensor, as a function of excess photon energy. Thin brown line: total $\mathbb{I}\mathrm{m}[\eta_I^{xxxx}]$ in GaAs; black, dashed red, and dotted blue lines: Ge; thin lines show only the current due to electron motion while thick lines include both hole and electron contributions.

$$\underset{(h)}{\mu_{I;e}^{abcde}}(\omega) = (-)\frac{i\pi e^3}{2\hbar^3\omega^3}\sum_{\substack{c,c',v\\(c,v,v')}}\int\frac{d^3k}{8\pi^3}\underset{(v'v)}{K_{cc'}^{ab}}(\mathbf{k})w_{cv}^{cd*}(\mathbf{k})\underset{(cv')}{v_{c'v}^{e}}(\mathbf{k})$$
$$\times(\delta[\omega_{cv}(\mathbf{k})-2\omega]+\delta[\underset{(cv')}{\omega_{c'v}}(\mathbf{k})-2\omega]), \quad (25)$$

where $K_{mn}^{ab}(\mathbf{k})$ is the spin-current matrix element between bands m and n at wave vector $\mathbf{k}$

$$\langle m\mathbf{k}|v^aS^b|n\mathbf{k}'\rangle = K_{mn}^{ab}\delta(\mathbf{k}-\mathbf{k}'). \quad (26)$$

It is evaluated from velocity and spin matrix elements, after inserting a resolution of unity between those operators on the left-hand side.

For zinc-blende and diamond structure crystals the spin-current injection pseudotensor $\mu_I^{abcde}(\omega)$ has six independent components and, in total, 54 nonzero elements. They are formed by cyclic permutations of the Cartesian indices and by the following relations

$$\mu_I^{xxxyz}=\mu_I^{xxyxz}=-\mu_I^{xxxzy}=-\mu_I^{xxzxy},$$

$$\mu_I^{xyzxx}=\mu_I^{xyxzx}=-\mu_I^{xzxyx}=-\mu_I^{xzyxx},$$

$$\mu_I^{xyzyy}=\mu_I^{xyyzy}=-\mu_I^{xzzyz}=-\mu_I^{xzyzz},$$

$$\mu_I^{xyzzz}=-\mu_I^{xzyyy},$$

$$\mu_I^{xyxxz}=-\mu_I^{xzxxy},$$

$$\mu_I^{xyyyz}=-\mu_I^{xzzzy}.$$

In Fig. 12, we show the calculated components for Ge.

C. Results

As an example, we consider the two-color field of Eq. (20) propagating along the $-\hat{\mathbf{z}}$ direction with our laboratory axes now aligned with crystallographic axes. The field components are given by $\mathbf{E}(\omega)=E_\omega e^{i\phi_\omega}\hat{\mathbf{e}}_\omega$ and $\mathbf{E}(2\omega)=E_{2\omega}e^{i\phi_{2\omega}}\hat{\mathbf{e}}_{2\omega}$, where $E_{\omega,2\omega}$ and $\phi_{\omega,2\omega}$ are real amplitudes and phases of the fields, and $\hat{\mathbf{e}}_{\omega,2\omega}$ their polarizations. We consider the cases of circular, colinear, and cross-linear polarizations.

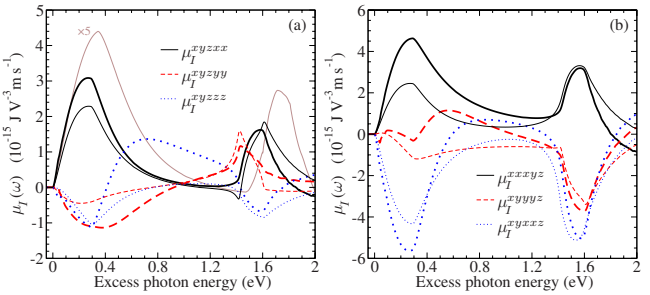

FIG. 12. (Color online) Components of the spin-current-injection pseudotensor $\mu_I^{abcde}(\omega)$ in Ge. Thin lines correspond to electron motion only; thick lines are the total injected current, including holes. The thin brown line in (a) shows the total μ_I^{xyzxx} in GaAs.

1. Circularly polarized beams

For cocircularly polarized beams of the same handedness, $\hat{\mathbf{e}}_{2\omega}=\hat{\mathbf{e}}_\omega=\hat{\boldsymbol{\sigma}}^{\mp}$, we get from Eqs. (22) and (24)

$$\dot{\mathbf{J}}_I=\frac{1}{\sqrt{2}}\mathbb{I}\mathrm{m}[\eta_I^{xxxx}-\eta_I^{xyyx}+2\eta_I^{xxyy}]E_\omega^2E_{2\omega}\hat{\mathbf{m}}, \quad (27)$$

$$\dot{K}_I^{ab}=\pm\frac{1}{\sqrt{2}}(\mu_I^{xyzzz}-\mu_I^{xyxxz}+2\mu_I^{xyxzx})E_\omega^2E_{2\omega}\hat{\mathbf{m}}^a\hat{\mathbf{z}}^b$$
$$\mp\frac{1}{\sqrt{2}}(\mu_I^{xyzzz}-\mu_I^{xyyyz}+2\mu_I^{xyyzy})E_\omega^2E_{2\omega}\hat{\mathbf{z}}^a\hat{\mathbf{m}}^b. \quad (28)$$

Equation (27) and the first term of Eq. (28) correspond to a spin-polarized current with $\hat{\mathbf{z}}$ as the polarization axis. The charge flow is along the direction $\hat{\mathbf{m}}$, given by $\hat{\mathbf{m}}=\hat{\mathbf{x}}\sin(\Delta\phi)\pm\hat{\mathbf{y}}\cos(\Delta\phi)$, where $\Delta\phi\equiv2\phi_\omega-\phi_{2\omega}$; $\Delta\phi$, a phase-matching parameter, controls the direction of the current. In Sec. III, we have seen how circularly-polarized monochromatic light injects a spin population in the sample. It is perhaps not so surprising, then, that the cocircularly polarized two-component field induces a spin-polarized current.

There is another contribution to the spin-current injection: the second term in Eq. (28) is associated with carriers moving along the axis of incidence with their spins polarized along $\hat{\mathbf{m}}$. This corresponds to a pure spin current since no net charge current is associated with this component. If we instead choose $\hat{\mathbf{e}}_\omega=\hat{\boldsymbol{\sigma}}^{\mp}$ to form opposite-circularly polarized beams, there is a change of sign for the contributions of $2\eta_I^{xxyy}$, $2\mu_I^{xyxzx}$, and $2\mu_I^{xyyzy}$ in the above expressions.

2. Colinearly polarized beams

With colinearly polarized beams, both along $\hat{\mathbf{x}}$, the rates of current and spin-current injection are

$$\dot{\mathbf{J}}_I = 2\mathbb{I}\mathrm{m}[\eta_I^{xxxx}]\hat{\mathbf{x}}E_\omega^2 E_{2\omega}\sin(\Delta\phi), \tag{29}$$

$$\dot{K}_I^{ab} = 2\mu_I^{xyzzz}(\hat{\mathbf{y}}^a\hat{\mathbf{z}}^b - \hat{\mathbf{z}}^a\hat{\mathbf{y}}^b)E_\omega^2 E_{2\omega}\cos(\Delta\phi). \tag{30}$$

We see that charge and spin currents are injected with their phase-matching conditions out of phase by $\pi/2$ so that one is at a maximum when the other vanishes. Within the independent particle approximation η_I is purely imaginary and μ_I is purely real, which leads to the difference in the phases that appear in Eqs. (29) and (30).

This configuration offers only a weak spin-current response due to the complete lack of helicity of the incident beams. Pure spin currents arise in the plane perpendicular to the polarization of the fields with a magnitude proportional to the small but nonzero pseudotensor component μ_I^{xyzzz} (*cf.* Fig. 12). At low excitation energy ($2\hbar\omega$ less than 0.4 eV above the absorption edge), the response is almost completely accounted for by the contribution from electrons alone. This is also true for the injection enhancement at 1.6 eV of excess photon energy, which stems from the large number of states available at this energy difference in the Γ-L valley. For mid-range photon energies, the electron contribution nearly vanishes, the hole contribution becomes important, and the total injected spin current is reversed; it reaches a maximum amplitude roughly 25% higher than the low-energy maximum.

Another component of the response to the colinear beams is the charge current injected parallel to the polarization axis with a magnitude proportional to η_I^{xxxx} (*cf.* Fig. 11).[50] As is commonly done,[45,51] we characterize the average velocity per injected carriers forming this current by introducing a swarm velocity, defined by

$$v_{\mathrm{s}}^x = \frac{\dot{J}^x}{e\dot{n}} \tag{31}$$

with $\dot{n}$ from Eq. (21). This quantity is maximized in the following way: first, we adjust the phases of the beams until $\Delta\phi$ is a multiple of $\pi/2$. Second, we adjust the intensities of the ω and 2ω beams so that the velocity in Eq. (31) is maximized; this occurs when the injection rates $\dot{n}_1(2\omega)$ and $\dot{n}_2(\omega)$ are equal. When this is done, the swarm velocity, using $\dot{J}^x$ from Eq. (29), takes its maximal value

$$v_{\mathrm{s,max}}^x(\omega) = \frac{\mathbb{I}\mathrm{m}[\eta_I^{xxxx}(\omega)]}{e\sqrt{\xi_1^{xx}(2\omega)\xi_2^{xxxx}(\omega)}}. \tag{32}$$

We show the maximal swarm velocity versus excess photon energy in Fig. 13. Excitations at the direct band-gap energy inject only stationary electrons at the Γ point but the swarm velocity increases quickly from zero to over 400 km/s within a couple hundred meV of the absorption edge. At the onset of transitions from the split-off band ($2\hbar\omega - E_{dg} = 0.29$ eV), slow-moving zone-center electrons are excited, bringing the average velocity down. They are injected only in a small number, however, and cannot account for the steady drop of the electron swarm velocity in the 0.5–1.4 eV range, culminating in a dip at 220 km/s. This is better explained by the "curving down" of the conduction band at these higher energies. Around the dip, which corresponds to a photon energy of $2\hbar\omega \approx 2.3$ eV, some electrons in the Γ-L direction of the Brillouin zone have zero injection velocities. Electrons excited by slightly more energetic photons stem predominantly from the high joint density of states associated with the E_1 and $E_1+\Delta_1$ absorption features. These have lesser velocities compared to electrons in the Γ-X direction, which make up for most of the injected current at high energies.

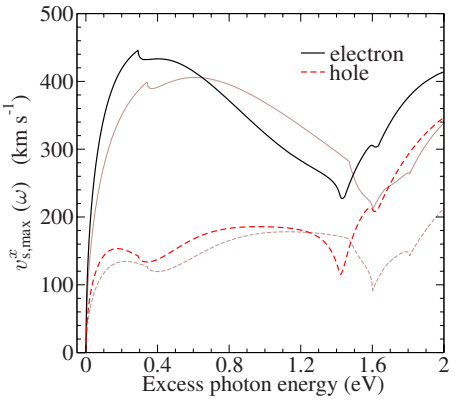

FIG. 13. (Color online) Maximal swarm velocity for the charge current injected with colinearly polarized ω and 2ω beams. Plain black, dashed red curves: electron and hole velocity in Ge; brown curves: electron and hole velocity in GaAs.

Injected holes are slower and have a much flatter velocity spectrum, which is also apparent simply by looking at their band dispersion. Low-energy holes, excited close to the Γ point, have a swarm speed of about 160 km/s, less than half the top electron speed, consistent with their larger average effective mass. Due to warping of the light-hole band only a few tens of meV above the absorption edge, the hole swarm velocity drops. When the excess photon energy matches the spin-orbit splitting, zone-center split-off holes are excited, also bringing the average velocity down. At high photon energies, holes are injected in the Γ-X direction of the Brillouin zone with large velocities; the current generated by the holes can be as much as 45% of the total current. Both contributions from electrons and holes are reinforcing the current over the entire energy range of our calculation.

3. Cross-linearly polarized beams

With cross-linearly polarized beams, ω along $\hat{\mathbf{x}}$ and 2ω along $\hat{\mathbf{y}}$, we get the following injection rates

$$\dot{\mathbf{J}}_I = 2\,\mathbb{I}\mathrm{m}[\eta_I^{xyyx}]\hat{\mathbf{y}}E_\omega^2 E_{2\omega}\sin(\Delta\phi), \tag{33}$$

$$\dot{K}_I^{ab} = 2(\mu_I^{xyyyz}\hat{\mathbf{z}}^a\hat{\mathbf{x}}^b - \mu_I^{xyxxz}\hat{\mathbf{x}}^a\hat{\mathbf{z}}^b)E_\omega^2 E_{2\omega}\cos(\Delta\phi). \tag{34}$$

The "cross-linear" configuration generates a strong pure spin current (PSC) along the ω-beam polarization axis with a magnitude determined by μ_I^{xyxxz} and a polarization parallel to the incident beams. Additionally, two weaker currents also occur: a charge current along the second harmonic polarization axis and another PSC along the axis of incidence. The magnitude of the charge current, given by η_I^{xyyx}, is very small for zone-center excitations. This tensor component is pre-

dicted to be null by a parabolic-band model; low-energy deviations from zero are due to band warping.[29] At higher energies, the assumption of parabolic bands is not even a good first approximation. Our calculation shows that there is a significant current arising from this tensor component when excess photon energy exceeds 1.4 eV with electrons and holes providing comparable contributions.

The smaller component of the spin-current response, proportional to μ_I^{xyyyz}, injects a pure spin current parallel with the axis of incidence. The electronic contribution to this component is zero at the onset of absorption and remains small even when excess photon energy is increased by a few hundred meV's. For $2\hbar\omega - E_{dg} \gtrsim 1.5$ eV, however, there is a strong contribution from electrons in the Γ-X direction of the Brillouin zone. The holes slightly reinforce the electron spin current at this enhancement and at Γ but otherwise their contribution has the opposite sign.

Let us now discuss the predominant spin-current response: the PSC along the ω-beam polarization axis with carriers spin polarized parallel to the incident beams. The associated pseudotensor component, μ_I^{xyxxz}, is particularly strong at an excess photon energy of 0.25 eV (where excitations from the split-off band are still excluded) and again at 1.5 eV. This PSC is dominated by electrons although there is a significant contribution from holes at low energies.

In a pure spin current, spin-up and spin-down carriers are moving in opposite directions. There is no overall spin injection along the polarization axis and the average carrier velocity along the axis associated with the movement of carriers is zero. Therefore, there is no expression for the swarm velocity of carriers forming a PSC that is directly analogous to Eq. (32) because there is no net current injection associated with the motion of carriers described by a spin current if it is pure. However, for a subset of the injected carriers the average velocity need not be zero. Recall, for example, the simpler process of one-photon absorption, where there is no injection of current. An electron, injected above the bottom of the conduction band at some wave vector $\mathbf{k}$, has a certain velocity determined from the slope of the band at that $\mathbf{k}$ point, while another, injected at $-\mathbf{k}$, has the same energy but opposite velocity. Only by averaging the microscopic velocities of carriers injected at $\mathbf{k}$ and $-\mathbf{k}$ do we arrive at the result of zero net current.

More generally, suppose one is calculating some response function $G(\omega)$, determined by a Brillouin-zone integration of the form

$$G(\omega) = \int \frac{d^3k}{8\pi^3} g(\mathbf{k}) \delta[\omega_{cv}(\mathbf{k}) - 2\omega]$$

similar to the spin, current, and spin-current injection tensors of this paper. Clearly the integral $G(\omega)$ can vanish even though the integrand $g(\mathbf{k})$ does not. By looking at contributions to $G(\omega)$ from different parts of the Brillouin zone, one can investigate the nature of the response. We use this strategy to better characterize the PSC in the cross-linear configuration. We cut the Brillouin zone in half at the yz plane (i.e., the plane normal to the direction of the spin current) and perform spin- and current-injection calculations over either of these halves. Our calculations confirm that carriers injected into the two halves (a) move in opposite directions and (b) have opposite average spin polarization. This correlation between motion and spin causes the PSC of Eq. (34) to materialize.

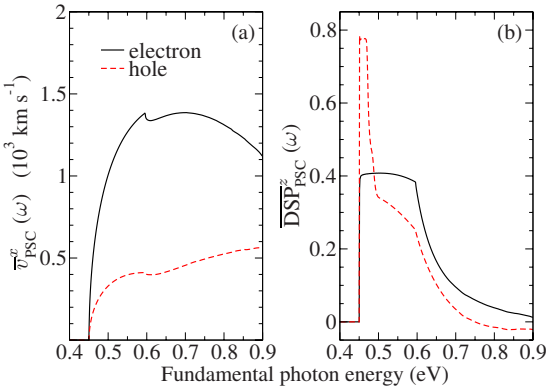

FIG. 14. (Color online) (a) Average velocity and (b) degree of spin polarization of positive-k^x carriers making up the pure spin current injected with cross-linearly polarized ω and 2ω beams. Carriers with negative k^x have the opposite polarization and velocity.

It is the interference of amplitudes from one- and two-photon absorption that gives rise to the spin injection in this experimental configuration

$$\dot{S}_I^z = 2\zeta_I^{zxxy} E_\omega^2 E_{2\omega} \cos(\Delta\phi), \tag{35}$$

where $\zeta_I = \zeta_{I;k^x\geq 0} + \zeta_{I;k^x\leq 0}$ is a purely real pseudotensor. In noncentrosymmetric semiconductors, ζ_I^{abcd} is a manifestation of spin population control,[29,52] but in Ge, ζ_I^{zxxy} vanishes. However, with a calculation including only the contribution from $\mathbf{k}$ points with positive k^x, a DSP analogous to Eq. (10) can be defined. We choose field amplitudes that maximize the spin-current injection and define

$$\overline{\rm DSP}^z_{\rm PSC}(\omega) = \frac{(\hbar/2)^{-1} 2\zeta^{zxxy}_{I;k^x\geq 0}(\omega)}{\sqrt{\xi_1^{xx}(2\omega)\xi_2^{xxxx}(\omega)}}. \tag{36}$$

Likewise, we introduce a measure of the swarm velocity of positive-k^x carriers

$$\bar{v}^x_{\rm PSC}(\omega) = \frac{\eta^{xyy}_{1;k^x\geq 0}(2\omega)}{e\xi_1^{xx}(2\omega)} + \frac{\eta^{xxxxx}_{2;k^x\geq 0}(\omega)}{e\xi_2^{xxxx}(\omega)}. \tag{37}$$

Here, η_1 and η_2 are tensors for single-beam current injection by one- and two-photon absorption, respectively. The former leads to the (bulk) circular photogalvanic effect, which vanishes in crystal of diamond and zinc-blende structures.[53] Its microscopic expression is given by van Driel and Sipe;[45] η_2 is constructed in a similar way.

The effective quantities of Eqs. (36) and (37) describe PSC injection. They are shown in Fig. 14. We find that by selecting carriers with a positive k^x, our calculation of the effective swarm velocity shows values that are close to three times larger than the maximal swarm velocity of Fig. 13 for the charge current, which includes all carriers. One has to

keep in mind that Eq. (37) takes into account only half of the injected carriers and that averaging over the whole Brillouin zone yields no net motion.

Our calculation of ζ_I^{zxxy} is performed with the multiple-scale approach to include coherences. We find that hole polarization is close to 80% at the onset of absorption. Breaking the calculation down into contributions from each valence band shows that light-hole polarization is 60% while heavy holes are fully polarized. The polarizations associated with these bands exhibit plateaus over ranges of roughly 40 and 25 meV, respectively. As photon energy is increased further, the combined DSP drops to roughly 35%. At higher energies, transitions involving the heavy-hole band yield electrons and holes with a mirrored polarization; the net spin polarization follows a slow monotonic decline, but does not change sign in the energy range presented here. The light-hole polarization drops more steeply and changes sign at $\hbar\omega \approx 670$ meV. This, combined with additional −25% polarized holes being injected into the split-off band for $\hbar\omega \geq 595$ meV, provides the decreasing average hole spin polarization visible in Fig. 14(b).

Electrons are injected with −40% polarization at the Γ point with roughly equal contributions from transitions originating from the heavy- and light-hole bands. As the excess photon energy increases from the band-gap energy, there is an increase in the spin polarization of electrons excited from the light-hole band. This rise almost exactly balances the decrease in polarization for the heavy-hole-mediated transitions, thus forming a plateau in the combined DSP for a wide range of low energies: $E_{dg} \leq 2\hbar\omega \leq E_{dg} + \Delta_{so}$. At the onset of absorption from the split-off band, electrons excited from the light-hole band exhibit decreasing polarization. Electrons excited from the split-off band have a strong opposite polarization (70%) and largely contribute to a sharp drop in the DSP. At higher energies, hole- and electron-spin polarizations follow the same decreasing trend.

V. CONCLUSION

We have performed calculations of optical spin, current, and spin-current injection in bulk germanium and have shown their spectral dependence. A wide range of excitation energy is covered, including the E_1 resonance, by virtue of the full-zone band structure offered by the 30-band $\mathbf{k}\cdot\mathbf{p}$ model. By comparison, previous studies were limited to a few hundred meV's above the band edge. Anisotropic effects in the band structure contribute to stronger two-photon carrier and spin injection for light incident on a ⟨111⟩ surface but the average spin per injected carrier is almost insensitive to the crystal orientation. We find that high spin injection is achieved at an excess photon energy 200 meV above the direct gap.

We also defined and computed effective measures of swarm velocity and polarization for pure spin currents. We argue that a PSC originates from correlated motion and polarization, and compute average velocity and spin for only a subset of carriers with positive crystal momentum along the direction of motion of the PSC. In the case of cross-linearly polarized, harmonically related beams incident on ⟨001⟩, we find that the spectral dependence of the carrier polarization is comparable to both one- and two-photon spin orientation, and that velocities are three times as large as typical swarm velocities of optically injected charge currents. For many of the current calculations, a centrosymmetric material has been considered for the first time. Such materials facilitate the study of coherently controlled interference currents experimentally since no one-beam currents occur.

For the effects presented here, the optical response of Ge resembles qualitatively that of GaAs. The magnitude of most response tensors are larger for Ge than for GaAs due to lighter effective masses in germanium. Perhaps the most significant difference comes from the side-valley relaxation mechanism in Ge; although injection processes are very similar for both semiconductors, we expect that the subsequent dynamics is not. The conduction-band minimum at the L point in Ge offers a relaxation process for injected electrons which gives greater access to holes. As a consequence, holes can be expected to play an important role and we have studied their contributions to the various injection tensors. Indeed, a recent measurement in Ge shows that the detected PSC signature relaxes on a much faster time scale than in GaAs although the technique could not determine whether the fast dynamics is due to electron intervalley scattering or hole spin-relaxation time.[3] Probing these effects in spin and current injection in Ge is a subject of ongoing experimental investigations.[4]

ACKNOWLEDGMENTS

This work is supported by FQRNT and NSERC of Canada. The authors wish to thank F. Nastos and A. Smirl for useful discussions, and A. Smirl for also providing us with a preprint of their current work. J.R. gratefully acknowledges G. Burkard and his research group for their hospitality while at Konstanz Universität.

[1] D. J. Hilton and C. L. Tang, Phys. Rev. Lett. **89**, 146601 (2002).
[2] Z. G. Yu, S. Krishnamurthy, M. van Schilfgaarde, and N. Newman, Phys. Rev. B **71**, 245312 (2005).
[3] E. J. Loren, B. A. Ruzicka, L. K. Werake, H. Zhao, H. M. van Driel, and A. L. Smirl, Appl. Phys. Lett. **95**, 092107 (2009).
[4] A. L. Smirl, E. J. Loren, B. A. Ruzicka, L. K. Werake, H. Zhao, and H. M. van Driel, OSA Technical Digest, *Conference on Lasers and Electro-Optics/International Quantum Electronics Conference* (Optical Society of America, Baltimore, 2009), paper IWA6.
[5] E. Yablonovitch, H. W. Jiang, H. Kosaka, H. D. Robinson, D. S. Rao, and T. Szkopek, Proc. IEEE **91**, 761 (2003).
[6] I. Žutić, J. Fabian, and S. Das Sarma, Rev. Mod. Phys. **76**, 323 (2004).

[7] *Modern Problems in Condensed Matter Sciences*, edited by F. Meier and B. P. Zakharchenya (North-Holland, Amsterdam, 1984), Vol. 8, Chap. 2, pp. 15–71.

[8] M. D. Dvorak, W. A. Schroeder, D. R. Andersen, A. L. Smirl, and B. S. Wherrett, IEEE J. Quantum Electron. **30**, 256 (1994).

[9] D. C. Hutchings and B. S. Wherrett, Phys. Rev. B **49**, 2418 (1994).

[10] D. C. Hutchings and B. S. Wherrett, Opt. Mater. **3**, 53 (1994).

[11] M. Murayama and T. Nakayama, Phys. Rev. B **52**, 4986 (1995).

[12] S. B. Arifzhanov and E. L. Ivchenko, Fiz. Tverd. Tela (Leningrad) **17**, 81 (1975) [Sov. Phys. Solid State **17**, 46 (1975)].

[13] G. W. Bryant, Phys. Rev. B **22**, 1992 (1980).

[14] A. F. Gibson, C. B. Hatch, P. N. D. Maggs, D. R. Tilley, and A. C. Walker, J. Phys. C **9**, 3259 (1976).

[15] E. Tuncel, J. L. Staehli, C. Coluzza, G. Margaritondo, J. T. McKinley, R. G. Albridge, A. V. Barnes, A. Ueda, X. Yang, and N. H. Tolk, Phys. Rev. Lett. **70**, 4146 (1993).

[16] C. Rauscher and R. Laenen, J. Appl. Phys. **81**, 2818 (1997).

[17] R. Atanasov, A. Haché, J. L. P. Hughes, H. M. van Driel, and J. E. Sipe, Phys. Rev. Lett. **76**, 1703 (1996).

[18] A. Haché, Y. Kostoulas, R. Atanasov, J. L. P. Hughes, J. E. Sipe, and H. M. van Driel, Phys. Rev. Lett. **78**, 306 (1997).

[19] A. Haché, J. E. Sipe, and H. M. van Driel, IEEE J. Quantum Electron. **34**, 1144 (1998).

[20] D. Côté, J. M. Fraser, M. DeCamp, P. H. Bucksbaum, and H. M. van Driel, Appl. Phys. Lett. **75**, 3959 (1999).

[21] M. Spasenović, M. Betz, L. Costa, and H. M. van Driel, Phys. Rev. B **77**, 085201 (2008).

[22] R. D. R. Bhat and J. E. Sipe, Phys. Rev. Lett. **85**, 5432 (2000).

[23] M. J. Stevens, A. L. Smirl, R. D. R. Bhat, J. E. Sipe, and H. M. van Driel, J. Appl. Phys. **91**, 4382 (2002).

[24] M. J. Stevens, A. L. Smirl, R. D. R. Bhat, A. Najmaie, J. E. Sipe, and H. M. van Driel, Phys. Rev. Lett. **90**, 136603 (2003).

[25] J. Hübner, W. W. Rühle, M. Klude, D. Hommel, R. D. R. Bhat, J. E. Sipe, and H. M. van Driel, Phys. Rev. Lett. **90**, 216601 (2003).

[26] S. Richard, F. Aniel, and G. Fishman, Phys. Rev. B **70**, 235204 (2004); **71**, 169901(E) (2005).

[27] R. D. R. Bhat, P. Nemec, Y. Kerachian, H. M. van Driel, J. E. Sipe, and A. L. Smirl, Phys. Rev. B **71**, 035209 (2005).

[28] R. D. R. Bhat, F. Nastos, A. Najmaie, and J. E. Sipe, Phys. Rev. Lett. **94**, 096603 (2005).

[29] R. D. R. Bhat and J. E. Sipe, arXiv:cond-mat/0601277 (unpublished).

[30] F. Nastos, R. W. Newson, J. Hübner, H. M. van Driel, and J. E. Sipe, Phys. Rev. B **77**, 195202 (2008)

[31] M. Cardona and F. H. Pollak, Phys. Rev. **142**, 530 (1966).

[32] G. F. Koster, J. O. Dimmock, R. G. Wheeler, and H. Statz, *Properties of the Thirty-Two Point Groups* (MIT Press, Cambridge, MA, 1963).

[33] By symmetry of the diamond structure, the nonzero momentum matrix elements are given by: $\langle S|p^x|X\rangle=\langle S|p^y|Y\rangle=\langle S|p^z|Z\rangle$, $\langle X|p^y|z\rangle=\langle Y|p^z|x\rangle=\langle Z|p^x|y\rangle=\langle X|p^z|y\rangle=\langle Y|p^x|z\rangle=\langle Z|p^y|x\rangle$, $\langle D_z|p^x|X\rangle=\langle D_z|p^y|Y\rangle=-\frac{1}{2}\langle D_z|p^z|Z\rangle=-\frac{1}{\sqrt{3}}\langle D_x|p^x|X\rangle=\frac{1}{\sqrt{3}}\langle D_x|p^y|Y\rangle$, and complex conjugates of these relations.

[34] Other nonzero spin-orbit terms are found according to the relation $\langle D_z|(\nabla V\times\mathbf{p})^x|x\rangle=\langle D_z|(\nabla V\times\mathbf{p})^y|y\rangle=-\frac{1}{2}\langle D_z|(\nabla V\times\mathbf{p})^z|z\rangle=-\frac{1}{\sqrt{3}}\langle D_x|(\nabla V\times\mathbf{p})^x|x\rangle=\frac{1}{\sqrt{3}}\langle D_x|(\nabla V\times\mathbf{p})^y|y\rangle$.

[35] This term is important in the determination of the Landé g^* factor (Refs. 30 and 38) but not critical for the calculations of this paper. It is included in many 14-band models (Refs. 9 and 36–38); its earliest introduction seems to date back to M. Cardona, F. H. Pollak, and J. G. Broerman, Phys. Lett. **19**, 276 (1965).

[36] M. Cardona, N. E. Christensen, M. Dobrowolska, J. K. Furdyna, and S. Rodriguez, Solid State Commun. **60**, 17 (1986).

[37] P. Pfeffer and W. Zawadzki, Phys. Rev. B **41**, 1561 (1990).

[38] N. Fraj, S. Ben Radhia, and K. Boujdaria, Solid State Commun. **142**, 342 (2007).

[39] F. Nastos, J. Rioux, M. Strimas-Mackey, B. S. Mendoza, and J. E. Sipe, Phys. Rev. B **76**, 205113 (2007).

[40] Z. H. Levine and D. C. Allan, Phys. Rev. Lett. **63**, 1719 (1989).

[41] Z. H. Levine and D. C. Allan, Phys. Rev. B **43**, 4187 (1991).

[42] *Semiconductors: Group IV Elements and III-V Compounds*, edited by O. Madelung (Springer-Verlag, New York, 1991).

[43] P. E. Blöchl, O. Jepsen, and O. K. Andersen, Phys. Rev. B **49**, 16223 (1994).

[44] For details of the germanium band structure, see Fig. 4 of Ref. 26.

[45] H. M. van Driel and J. E. Sipe, in *Ultrafast Phenomena in Semiconductors*, edited by K.-T. Tsen (Springer-Verlag, Berlin, 2000), Chap. 5, pp. 261–306.

[46] C. R. Pidgeon, B. S. Wherrett, A. M. Johnston, J. Dempsey, and A. Miller, Phys. Rev. Lett. **42**, 1785 (1979); **43**, 1843(E) (1979).

[47] G. Jalbert, H. S. Brandi, B. Koiller, and N. Zagury, Opt. Commun. **65**, 213 (1988).

[48] I. M. Catalano, A. Cingolani, R. Cingolani, and M. Lepore, Phys. Scr. **37**, 579 (1988).

[49] J. M. Fraser, A. I. Shkrebtii, J. E. Sipe, and H. M. van Driel, Phys. Rev. Lett. **83**, 4192 (1999).

[50] This is the simplest orientation. For the same crystal cut, one can get a slightly larger current injection with beams polarized along $\langle 110\rangle$; the largest current injection is achieved with beams polarized along $\langle 111\rangle$ (Ref. 29). We choose to present $\langle 100\rangle$ polarization results to keep the expressions simple.

[51] J. E. Sipe, A. I. Shkrebtii, and O. Pulci, Phys. Status Solidi A **170**, 431 (1998).

[52] M. J. Stevens, R. D. R. Bhat, J. E. Sipe, H. M. van Driel, and A. L. Smirl, Phys. Status Solidi B **238**, 568 (2003).

[53] V. M. Asnin, A. A. Bakun, A. M. Danishevskii, E. L. Ivchenko, G. E. Pikus, and A. A. Rogachev, Solid State Commun. **30**, 565 (1979).